

Optical Design of the Atacama Cosmology Telescope and the Millimeter Bolometric Array Camera

J. W. Fowler¹, M. D. Niemack¹, S. R. Dicker², A. M. Aboobaker^{1,5}, P. A. R. Ade³, E. S. Battistelli⁴, M. J. Devlin², R. P. Fisher¹, M. Halpern⁴, P. C. Hargrave³, A. D. Hincks¹, M. Kaul², J. Klein², J. M. Lau¹, M. Limon², T. A. Marriage^{1,6}, P. D. Mauskopf³, L. Page¹, S. T. Staggs¹, D. S. Swetz², E. R. Switzer¹, R. J. Thornton², C. E. Tucker³

¹ *Princeton University Department of Physics,
Jadwin Hall, Washington Road, Princeton, New Jersey 08544, USA*

² *University of Pennsylvania Department of Physics and Astronomy,
David Rittenhouse Laboratory, 209 South 33rd Street, Philadelphia, Pennsylvania 19104,
USA*

³ *Cardiff University School of Physics and Astronomy,
Queens Buildings, 5 The Parade, Cardiff CF24 3AA, Wales, United Kingdom*

⁴ *University of British Columbia Department of Physics and Astronomy,
6224 Agricultural Road, Vancouver, British Columbia V6T 1Z1, Canada*

⁵ *Present Address: University of Minnesota School of Physics and Astronomy,
116 Church St. SE, Minneapolis, Minnesota 55455, USA*

⁶ *Present Address: Princeton University Department of Astrophysical Sciences,
Peyton Hall, Ivy Lane, Princeton, New Jersey 08544, USA*

jfowler@princeton.edu

The Atacama Cosmology Telescope is a 6-meter telescope designed to map the Cosmic Microwave Background simultaneously at 145 GHz, 215 GHz, and 280 GHz with arcminute resolution. Each frequency will have a 32 by 32 element focal plane array of TES bolometers. This paper describes the design of the telescope and the cold reimaging optics, which is optimized for millimeter-wave observations with these sensitive detectors. © 2019 Optical Society of America

OCIS codes: 040.1240, 080.3620, 350.1260

1. Introduction

The Atacama Cosmology Telescope (ACT)¹ will observe the oldest light in the universe, the cosmic microwave background (CMB), mapping it on arcminute to degree scales. The CMB is relic thermal radiation released when the early universe had cooled enough for the primordial plasma to form a neutral gas, allowing light to stream freely ever since. The CMB’s blackbody spectrum has redshifted with the expansion of the universe to a present temperature of 2.7 K. The temperature is uniform to tens of parts per million. Recently, the Wilkinson Microwave Anisotropy Probe (WMAP)² has measured the CMB power spectrum (the amplitude of temperature fluctuations in the CMB as a function of angular scale) at resolutions as fine as 0.3° . The data from WMAP in conjunction with other experiments^{3–7}—some at higher resolution—permit estimates of the universe’s global curvature and other properties with unprecedented precision.⁸

Maps of the CMB with high resolution from ACT—combined with optical, ultraviolet and X-ray measurements—will further constrain inflationary models of the early universe, constrain the equation of state of dark energy in the universe, probe light neutrino masses down to $m_\nu \simeq 0.1$ eV, and map the mass distribution of the universe.^{9–11} Such science will require measurements of the CMB temperature in multiple frequency bands near the null in the Sunyaev-Zel’ovich (SZ) effect¹² spectrum (217 GHz) to a precision of a few microkelvin at resolutions approaching one arcminute. Arcminute resolution at these frequencies requires telescopes in the 5 to 10 meter range. As a compromise between cost and angular resolution, ACT has a 6-meter (projected diameter) primary mirror. In this paper we outline the optical design that we have developed to meet our science requirements.

Around 217 GHz, atmospheric absorption permits observations only at high, dry sites. The Atacama plateau in northern Chile offers an excellent combination of observing conditions, sky coverage, and accessibility and was selected as the site for ACT. The telescope described here has been built, and it has been shipped to Chile from its construction site in Port Coquitlam, British Columbia.

2. Telescope and camera overview

Meeting the ACT science goals requires extreme sensitivity, better than ten microkelvin rms uncertainty in map pixels of three square arcminutes. Even with sensitive modern millimeter-wave detectors, large focal planes containing many hundreds of detectors, months of integration time, and careful control of systematics are all essential. This section discusses the major requirements and features of our approach, which are summarized in Table 1.

The fundamental requirement of the ACT and MBAC optics design is that the telescope and camera must reimage the sky onto a focal plane filled with detectors ~ 1.0 mm in size, and that the image be diffraction-limited. The design is subject to geometric limitations on

Table 1. Requirements and features of the ACT optics.

Warm Telescope Optics
<ul style="list-style-type: none"> • Clear aperture (off-axis optics) to minimize scattering and blockage. • 6-meter primary mirror and 2-meter (maximum) secondary mirror diameters. • Very fast primary focus ($F \leq 1$) to keep the telescope compact. • Large (1.0°) and fast ($F \sim 2.5$) diffraction-limited focal plane. • Ground loading (due to spillover) smaller than atmospheric loading. • Space for structure and cryogenics between primary mirror and Gregorian focus. • Entire telescope must scan several degrees in azimuth at 10 cycles per minute.
Cold Reimaging Optics for MBAC
<ul style="list-style-type: none"> • Bandpasses 20–30 GHz wide, centered near 145, 215, and 280 GHz. • Approximately $22'$ square field of view in each band. • Diffraction-limited resolution on three 34 mm by 36 mm arrays. • Well-defined Lyot stop in all bands to maximize illumination of the primary. • Ghost images due to stray light no brighter than the diffraction-limited sidelobes.

the size and separation of the mirrors. Control of stray light is also of particular importance, since the ACT detectors will be used without feedhorns. Spillover radiation from the ground around the telescope must be prevented from reaching the detectors, and reflections and scattering within the optics must be minimized.

CMB experiments deliberately modulate their sensitivity to cosmic signals in order to reduce the impact of drifts in detector response, such as $1/f$ noise. Typical modulation methods involve using an optical chopping mirror or scanning the entire telescope in azimuth. In either case, the telescope beam moves rapidly back-and-forth on timescales faster than the $1/f$ knee of any low-frequency noise. We chose the scanning method, because it avoids a chopping flat’s most intractable scan-synchronous variations, including primary beam shape, ground pickup pattern, and mirror emission. Our normal observing mode will be to scan the 50-ton telescope in azimuth over a 5° range repeating every 5 to 6 seconds, while holding the elevation fixed (typically at 48°). This motion places considerable rigidity requirements on the telescope structure (see Section 5.C). Observing at fixed elevation ensures that the large gradient in atmospheric emission enters the camera as a constant addition, not as an AC term synchronized with the signal. To maintain a constant speed for as much of the scan as possible, we have aimed for brief acceleration periods of 300 ms at either end of each scan.

ACT will make simultaneous observations at 145, 215, and 280 GHz to distinguish vari-

ations in the primordial CMB from secondary anisotropies such as SZ galaxy clusters and foregrounds such as galactic dust and point sources.¹³ ACT’s receiver, the Millimeter Bolometric Array Camera (MBAC) will contain a 32×32 array of transition edge sensor (TES) bolometers^{14,15} at each of the three frequencies. The arrays will be cooled to 0.3 K by a closed-cycle helium-3 refrigeration system.^{16,17} Because the TES detectors are bolometric, the ACT optics must also have optical filters to define the bandpass for each camera.

The ACT detectors are 1.05 mm square and are spaced on a 1.05 mm (horizontal) by 1.15 mm (vertical) grid. Detectors aimed less than half a beamwidth apart on the sky fully sample the field of view in a single pointing. This is advantageous for minimizing detector and atmospheric noise in mapmaking,¹⁸ and ACT detectors reach this ideal at the lower frequencies. The effective focal length is 5.2 m for all arrays, giving a detector spacing of 44'' (horizontal) and 48'' (vertical) on the sky. This spacing is half the expected beam size at 145 GHz. The use of a fast focus at the detectors will allow MBAC to map the sky rapidly without compromising diffraction-limited imaging performance.

3. Gregorian telescope optics

The two-reflector Atacama Cosmology Telescope was optimized to have the best possible average performance across a square-degree field of view by varying the mirror shapes, angles, and separation. This compromise balances the various classical telescope aberrations for point images against each other. The design process for ACT used both analytic and numerical methods. Numerical methods alone might seem sufficient, because the end result of a global optimization is independent of the starting design. But the telescope parameter space is large and complicated, and we found it critical to enter the numerical stage with a good analytic design. We used the Code V optical design software¹⁹ to optimize the telescope design and to analyze its performance.

Our initial analytic designs met the Dragone condition^{20,21} to minimize astigmatism, following the implementation of Brown and Prata.²² This condition also minimizes geometrical cross-polarization.²³ A comparison of Gregorian and Cassegrain solutions showed that in otherwise equivalent systems, the Gregorian offered more vertical clearance between the secondary focus and the rays traveling from the primary to the secondary mirror. The extra clearance leaves more space for our $\sim 1 \text{ m}^3$ cryostat, so the Gregorian was chosen for ACT.

A simple Gregorian telescope satisfying the Dragone condition did not meet the diffraction-limited field of view requirement, but it was taken as the starting point for the numerical stage. The system was optimized by minimizing the rms transverse ray aberration at field points across the focal plane. Six design parameters were allowed to vary: the two conic constants, the relative tilt of the primary and secondary axes, the secondary radius of curvature, and the location and tilt of the Gregorian focal plane. The primary focal length was

fixed at exactly 5 m to keep the telescope compact. We found that requiring the primary and secondary mirrors to be coaxial did not substantially degrade image quality, so we imposed this constraint to simplify manufacturing and alignment of the telescope.

Our final design approximates an ideal aplanatic Gregorian telescope, a system with no leading-order spherical aberration or coma in the focal plane.²⁴ Strehl ratios S were estimated by calculating σ , the rms optical path variation over a large bundle of rays, and taking²⁵ $\ln S \approx -(2\pi\sigma)^2$. Over a 1.0° square field at the Gregorian focus, the Strehl ratio everywhere exceeds 0.9 at 280 GHz.

Table 2. Atacama Cosmology Telescope mirror shapes.^a

Mirror	z_{vert} (m)	R (m)	K	y_0 (m)	a (m)	b (m)
Primary	0.0000	-10.0000	-0.940935	5.000	3.000	3.000
Secondary	-6.6625	2.4938	-0.322366	-1.488	1.020	0.905
Gregorian focus ^b	-1.6758					

^a Equation 1 gives the full shapes; parameters and axes are defined in the text.

^b Best-fit focal plane location for objects at infinity.

The two mirrors are off-axis segments of ellipsoids in the final ACT design. Figure 1 contains mechanical drawings, while Figure 2 presents a ray trace and shows the z and y axes. The parameters of each mirror are listed in Table 2. Both shapes can be described by

$$z(x, y) = z_{\text{vert}} + \frac{(x^2 + y^2)/R}{1 + \sqrt{1 - (1 + K)(x^2 + y^2)/R^2}}, \quad (1)$$

where z is along the shared axis of symmetry (see axes on Figure 2), z_{vert} is the vertex position (the primary vertex defines $z=0$), R is the radius of curvature at the vertex, the conic constant $K = -e^2$, and e is the ellipsoid eccentricity. The usable region of each mirror is bounded by an elliptical perimeter. When projected into the xy plane, these boundaries are centered at $(x, y) = (0, y_0)$ and have semi-major and semi-minor axes of a and b in the x and y directions, respectively. The primary projection is circular, with $a = b$.

Diffraction at the small aperture stop (in the cryogenic camera) can lead to systematic errors, particularly if it loads the detectors with radiation emitted by ambient-temperature structures near the two mirrors. To minimize this spillover effect, each mirror is surrounded by a reflective aluminum “guard ring.” The rings ensure that radiation reaching the detectors from beyond the geometric footprints on each mirror comes mainly from the cold sky.

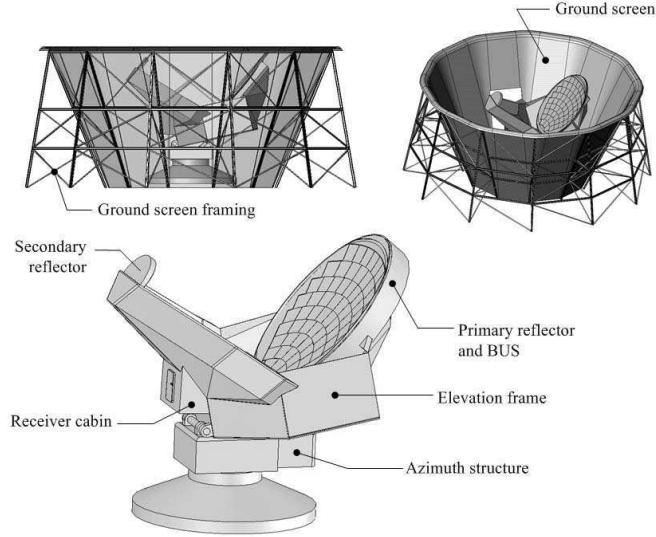


Fig. 1. The ACT telescope. The mechanical design has a low profile; the surrounding ground screen completely shields the telescope from ground emission. The screen also acts as a weather shield. An additional ground screen (not shown) mounted on the telescope hides the secondary and half the primary from the vantage point of the lower diagram. This inner ground screen is aluminum painted white to reduce solar heating. The primary mirror is ~ 7 m in diameter including its surrounding guard ring. “BUS” refers to the mirror’s back-up structure. (Figure credit: AMEC Dynamic Structures)

The ACT design also ensures that there is at least one meter of clearance between any ray approaching the secondary and the top of the Gregorian focal plane used by MBAC. The clearance allows room for a receiver cabin that will protect the cryostat and its supporting electronics from the harsh environment of the Atacama desert.

AMEC Dynamic Structures has designed, modeled, and built the telescope’s mechanical structure.²⁶ KUKA Robotics provided motion control.²⁷ The primary mirror and secondary surfaces consist of 71 and 11 aluminum panels, respectively. Forcier Machine Design²⁸ produced all of the panels. The panels are found to have a typical rms deviation from their nominal shapes of only $2\text{--}3\ \mu\text{m}$. We measure the positions of all the panel surfaces relative to telescope fiducial points with a Faro laser tracking system.²⁹ Four manually adjustable screw-mounts on the back of each panel then permit precise repositioning. To date, we have aligned the secondary panels to approximately $15\ \mu\text{m}$ rms. A subset of twelve primary panels has also been aligned to $30\ \mu\text{m}$ rms and monitored in detail over two twenty-four hour peri-

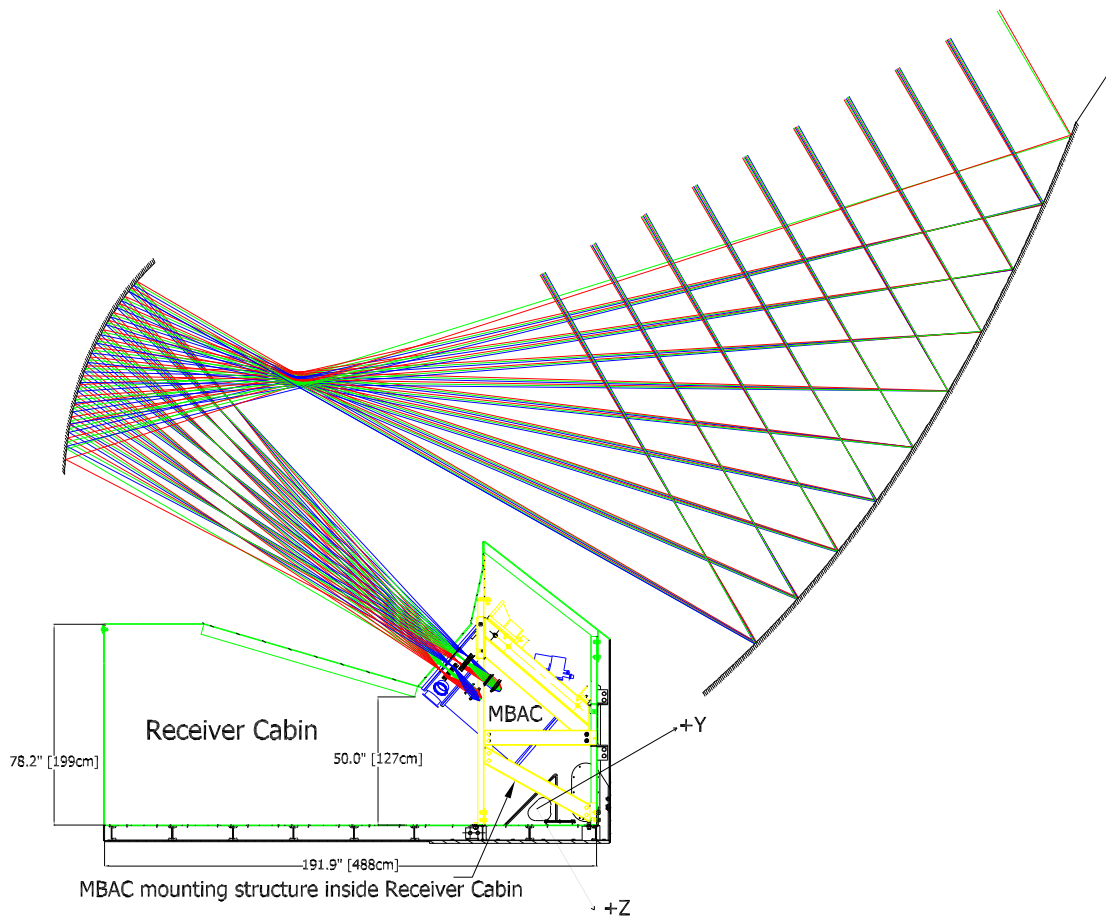


Fig. 2. (Color online) Rays traced into the MBAC cryostat (mounted at the far right of the receiver cabin). The stowed position is shown, corresponding to an elevation of 60° (generally, observations will be in the 40° – 50° range). The rays are traced from the central, highest, and lowest fields in the 280 GHz camera (higher in the cryostat) and the 215 GHz camera. Both the 215 GHz camera and the 145 GHz camera (not shown) lie outside the $x = 0$ midplane, relieving any apparent conflicts between filters and lenses from different cameras. The figure also shows the size and shape of the ACT receiver cabin, as well as the coordinate axes of Equation 1.

ods. We find that the primary expands thermally as if it were a single aluminum structure, except for mirror panels directly illuminated by the sun. We intend to adjust the mirror facets annually, if necessary.

Considerable effort has gone into ensuring the best possible performance for the azimuthal scanning of the telescope, a difficult task given its size and weight (~ 50 tons). The telescope meets the scanning target of $\pm 2.5^\circ$ at an angular speed of $2.0^\circ/\text{s}$ with a turn-around time of 300 ms. Encoders mounted on the azimuthal and elevation axes give 27-bit readings of the telescope orientation. We have found that the accuracy of pointing during scans is better than $4''$. Turn-arounds cause vibrations in the structure which induce brief $\sim 8''$ “shuddering” movements in elevation and an unavoidable $\sim 10''$ “bounce” in azimuth, due to the finite bandwidth of the drive servos. The azimuth bearing is driven by a pair of counter-torquing helical gears, eliminating backlash. The elevation errors occur only during the accelerations, while the azimuth bounce damps out exponentially $\tau \approx 200$ ms after the acceleration ends. Studying a large number of successive scans has shown that the rms deviation from the average scan shape is no more than $6.5''$ with 400 Hz sampling, demonstrating good repeatability of the scan pattern.

ACT’s compact design minimizes accelerations of the secondary and especially the cryogenics (which are near the rotation axis), simplifying mechanical design and helping to maintain refrigerator stability. The fast Gregorian focus ($F \sim 2.5$) keeps the vacuum window for the detector cryostat from being too large. Figure 2 shows the size and shape of the receiver cabin.

Actuators can move the secondary mirror structure in the y and z directions by ± 1 cm from the nominal position and can tilt it up to $\pm 1^\circ$ vertically or horizontally. We anticipate having to refocus in response to changes in ambient temperature or observing angle. We plan to operate the actuators as infrequently as possible, consistent with holding the primary-secondary distance to within $\pm 100 \mu\text{m}$ of nominal.

4. Cold reimaging optics in MBAC

Many possible architectures for the cold optics were studied, including all-reflecting designs, all-refracting designs, and hybrids of the two. We also compared designs of a single camera having dichroic filters to segregate the frequencies against a three-in-one camera design using a separate set of optics for each frequency. The final MBAC design uses only refractive optics instead of mirrors and employs the three-in-one approach.

4.A. MBAC architecture

Off-axis reimaging mirrors were studied by combining the equivalent paraboloid approximation³⁰ with the Dragone condition,²² then explored through numerical optimization. They

were rejected because the twin demands of image quality and a wide field-of-view led to designs too large to fit in a cubic-meter cryostat. For off-axis mirrors, the compromises between image quality and access to a cold image of the primary were also unacceptable. On-axis mirrors violated the requirement of an unobstructed aperture.

We have built dichroic beamsplitting filters as large as 15 cm diameter and metal mesh filters up to 30 cm diameter.³¹ Dichroics reflect one band and therefore must be flat to $\sim \lambda/40 \approx 25 \mu\text{m}$ at 280 GHz. Our optical designs required dichroics larger than any so far produced, and we considered their production and mounting too great a risk.

We chose a camera architecture with a separate set of cold lenses for each frequency, eschewing both cold mirrors and dichroic beamsplitters. There are several advantages of this design: anti-reflection coatings and capacitive mesh filters generally have higher transmission—and the designs are easier to optimize—for narrow bands; the mechanical design is simpler, more compact, and easier to align; and the three cameras are modular and can be removed from the cryostat as separate units for easy maintenance or for deploying MBAC in stages. The disadvantage is that each frequency observes a different area of sky; maps made with separated cameras do not completely overlap.

A triangular configuration was chosen for the three cameras (Figure 3) because it packs the cameras as close as possible to the field center, where the Gregorian image quality is best (as measured by Strehl ratio). The close packing also maximizes the overlap of observations. The 280 GHz camera is centered on the telescope’s plane of symmetry because it has the tightest diffraction requirements. The 215 GHz and 145 GHz cameras are placed symmetrically below it, allowing us to use a single design for the two lower-frequency lens sets. All the lenses within each camera are concentric and parallel, while the focal plane and the bolometer arrays are tilted by 8° or 5° .

4.B. Camera components

Figure 3 shows all three MBAC cameras. Separate vacuum windows are used for each camera. The windows are made of ultra-high molecular weight polyethylene (UHMWPE) and have anti-reflection (AR) coatings appropriate to their respective wavelengths. Light entering the camera module passes through an ambient-temperature infrared blocking “thermal” filter³² (mounted just inside the vacuum window) and three capacitive mesh filters cooled to 40 K (marked “LP” in Figure 3); two of the three are thermal filters, and one is a millimeter-wave low-pass filter. Together, these filters reduce blackbody loading on the colder stages and block out-of-band leaks in the bandpass filter (“BP”). A plano-convex silicon lens (Lens 1) creates an image of the primary mirror near lens 2. An assembly holds Lens 2 and two final low-pass filters at 1 K and contains a cold aperture stop (Lyot stop). The last two plano-convex silicon lenses (Lenses 2 and 3) refocus the sky onto the array. The bandpass filter

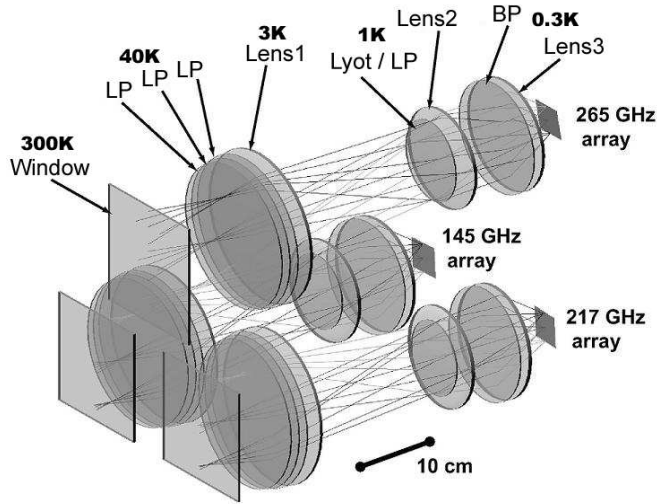


Fig. 3. The cold MBAC reimaging optics. Each frequency has a similar set of lenses and filters. The 280 GHz silicon lenses are labeled Lens 1 to 3 (with Lens 1 closest to the window). Infrared-blocking and low-pass capacitive mesh filters are all labeled LP; the bandpass filter is labeled BP. An IR-blocking filter (not shown) is also integrated into the window assembly. The temperatures of the components decrease away from the window as indicated. The bandpass filter, Lens 3, and the array are held at 0.3 K.

stands between these lenses, where the beam is slow enough for the filter to be effective. Lens 1 is cooled to 3 K; Lens 2 and the associated filters are cooled to 1 K; Lens 3 and the bandpass filter are cooled to 0.3 K. The unobstructed circular aperture of each element is large enough so that the outermost ray that can strike any detector passes at least five wavelengths from the aperture's edge, with the intentional exception of the Lyot stop. The entire camera is contained in a light-tight tube with cold black walls to absorb stray light. The walls are blackened with a mixture of carbon lampblack and Stycast 2850 FT epoxy.³³ All walls between the bandpass filter and the array are held at the coldest available temperature, 0.3 K, because their emission reaches the detectors without filtering.

Silicon was chosen as the lens material because of its high thermal conductivity and high refractive index ($n=3.416$ at 4 K).^{34,35} Pure, high-resistivity silicon ($\rho > 5000 \Omega\cdot\text{cm}$) is necessary to minimize absorption loss. Silicon of very low conductivity and low millimeter-wave loss must be made by the float zone process rather than by the more common (and less expensive) Czochralski process. Float zone silicon is available³⁶ in diameters up to 20 cm, restricting our clear aperture size to 19 cm. Alternative materials considered for the ACT

lenses included high density polyethylene (HDPE), crystalline quartz, fused quartz, and sapphire. Quartz and sapphire are both more expensive to buy and more difficult to cut than silicon. Optical designs were made using HDPE as a backup option. However, the plastic designs have substantially poorer image quality, a result of making large deflections with a less refractive material. Also, the lower-index HDPE required much thicker lenses and consequently higher absorption loss.

When using high refractive index materials, such as silicon, anti-reflective coatings are critical. We have developed a method for AR-coating silicon with quarter-wave layers of Cirlex ($n=1.85$).³⁷ Test samples show reflectivities less than 0.5% and transmission exceeding 95% per sample. We expect that the three lenses in each camera will absorb a combined 15% of incident light, predominantly in the Cirlex coating. Because of the corresponding emissivity in the lenses and their coatings, it is necessary to cool the lenses cryogenically, reducing the power they emit.

Plano-convex lenses are used so that only one face of each lens must be machined. The curved figures are surfaces of revolution of conic sections plus polynomial terms in r^4 , r^6 , r^8 and r^{10} to give maximal design freedom. As the lenses were diamond turned on a computer-controlled lathe, there was no cost penalty for adding axially symmetric terms to the lens shapes. The curved and flat surfaces of each lens were oriented so as to minimize reflection-induced secondary (“ghost”) images (see Section 5.D).

4.C. Design procedure

The Gregorian telescope design was held fixed during the cold optics design process, while the lens shapes and positions were varied. The 280 GHz and 215 GHz cameras were optimized separately. Because the 145 GHz and 215 GHz cameras are placed symmetrically about the telescope’s symmetry plane—and because there is no evidence for appreciable dispersion in silicon at millimeter wavelengths—the two design problems are mathematically equivalent; a single camera design was used for both.

The optimization method for the camera was similar to the method used to design the Gregorian telescope, but with additional constraints. Most importantly, we required a faithful image of the primary mirror in each camera at which to place a Lyot stop. This image quality was quantified by tracing rays from all field points through four points on the perimeter of the primary mirror. The rms scatter of such ray positions where they crossed the Lyot stop plane, projected onto the radial direction, was added to the cost function. Thus, an astigmatic image of the primary elongated tangent to the stop was not penalized, but a radial blurring was. This additional cost parameter measures the radial ray aberration at the aperture stop.

A second constraint was the effective focal length, fixed at 5.2 meters by checking the plate scale for points near the center of each sub-field. Finally, we found it necessary to require that

the chief ray from each field strike the focal plane at no greater than a 7° angle, which keeps the tilt of the detector plane small to maximize absorption in the detectors. This low-tilt requirement also produces an approximately telecentric image, meaning that the exit pupil is large and far from the detector plane. A telecentric image has the advantage that the plate scale does not depend to first order on the relative positioning of the detector array and the lenses.

The optimizer varied up to 27 parameters in each design: three lens positions along the optic axis, the position of the Lyot stop and its tilt, the detector position and tilt, and the lens shapes (parameters included curvature, conic constant, and four aspheric polynomial terms). We found that tilting the Lyot stop surface did not offer enough advantage to justify the added mechanical complication and thereafter did not allow it to tilt, reducing the number of parameters to 25. The center thickness of each lens was set by requiring the edge to be at least 2 mm thick for mechanical strength; center thickness was not varied by the optimizer. We did not constrain the dimensions of the elliptical Lyot stop. Striking the right balance in the cost function between optimizing the image of the sky at the detector plane and the image of the primary at the Lyot stop was challenging. Our most successful approach to meeting both goals simultaneously was to make two optimizing passes. In the first pass, the Lyot stop image was given large weight. In the second, it was given zero weight, but all parameters that affect the stop image were fixed (including shape and placement of L1 and placement of the stop).

The MBAC cold optics design is somewhat unusual in its use of cryogenic, AR-coated silicon lenses. For this reason, we have built a prototype 145 GHz receiver (CCam, the “column camera”) with a cold optics design based on the same principles as MBAC. We have tested CCam with a 1.5 m telescope and used it successfully to observe astronomical sources,³⁸ giving us confidence in the soundness of the general design of MBAC.

5. Design evaluation

The full optical design was studied using both ray-tracing and physical optics. Most analyses were first developed for the Penn Array Receiver at the Green Bank Radio Telescope.³⁹ We present the studies most relevant to deployment, calibration, and data analysis for ACT.

5.A. Image quality

The median Strehl ratios across the fields in the final design are calculated to be 0.991, 0.980, and 0.983 at 145, 215, and 280 GHz, respectively (Figure 4). The lowest Strehls corresponding to any of the 225 field points tested in each camera are 0.971 (145 GHz), 0.939 (215 GHz), and 0.958 (280 GHz). This performance is the baseline for comparison in the tolerance analysis (Section 5.C). These Strehl ratios establish that all points in the field of

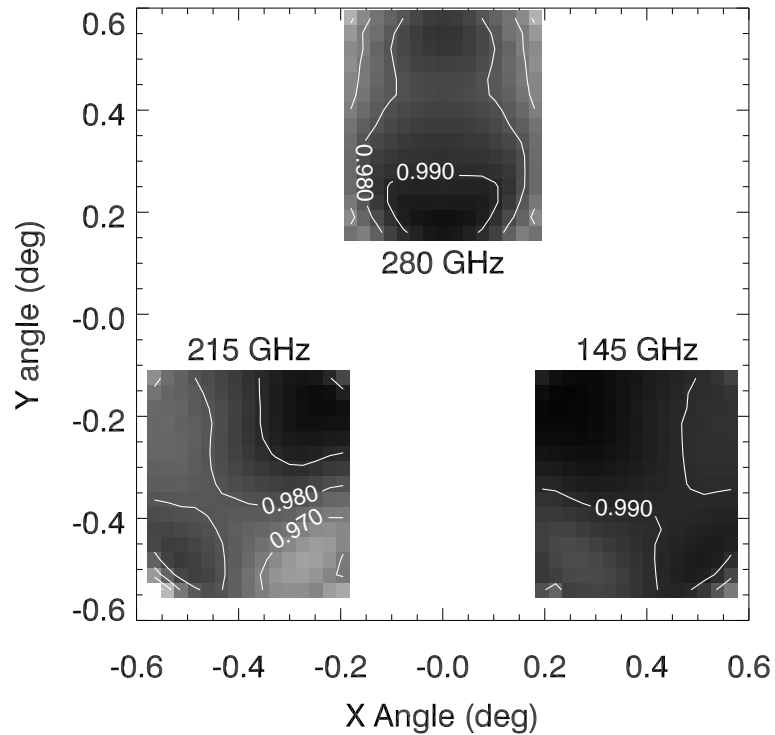


Fig. 4. Strehl ratio at points in the three ACT fields, as a function of field angle on the sky. The rectangular aspect of the focal plane array is primarily responsible for the departure from square fields, but anamorphic field distortion also contributes. The figure also indicates the relative spacing and size of the three fields. The median Strehl ratios are 0.983, 0.980, 0.991 for the 280, 215, and 145 GHz cameras.

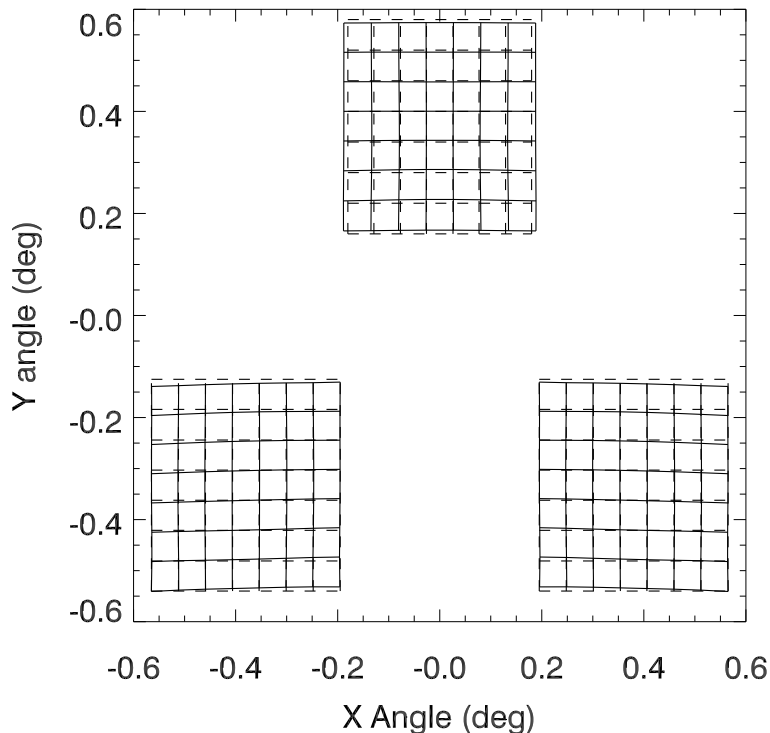


Fig. 5. Field distortion for the ACT optical design. The dashed square boxes depict a notional rectangular grid of field points on the sky, without distortion; the solid lines indicate the image of the same grid after it is refocused at the detectors (assuming the nominal 5.20 m effective focal length).

view will be diffraction-limited.

A small amount of field distortion results from reimaging such a large focal plane (Figure 5). One effect is anamorphic magnification, or horizontal image stretching: the plate scale in all cameras is 6.8' per cm for vertical separations, but for horizontal separations it is only 6.4' per cm in the 280 GHz camera and 6.6' per cm in the others. The other effect is a shearing of the image in the 145 and 215 GHz cameras; lines of constant elevation are twisted by approximately 1.4° with respect to horizontal rows of detectors. There is no appreciable rotation of lines of constant azimuth. These distortions will be taken into account in making CMB maps from the data, but at the predicted levels, they will not complicate our observations.

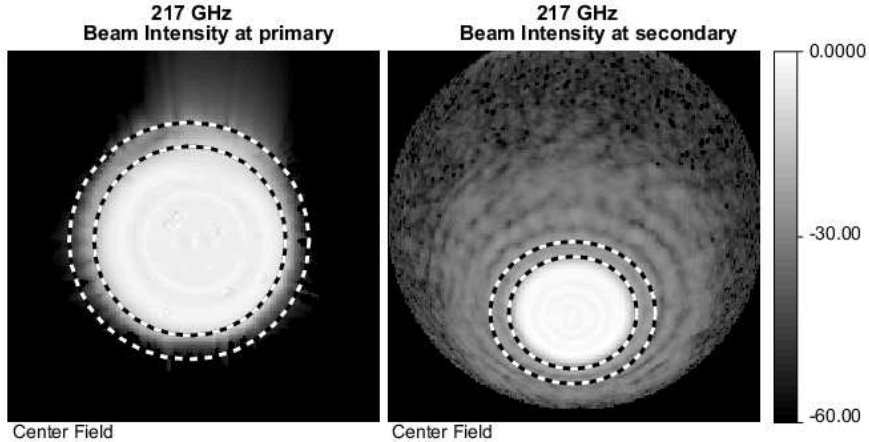


Fig. 6. The calculated illumination patterns of the primary (*left*) and secondary (*right*) mirrors projected into the (x, y) plane for the central 215 GHz detector. The inner dashed circles show the edge of the mirrors and the outer ones show the guard ring. Fine-scale structure in the right panel is an artifact of numerical precision and finite sampling, but all other structure is real. (Units are dB below peak level.)

5.B. Stop size and spillover

The size of the elliptical Lyot stop was chosen to illuminate only 97% of the primary mirror diameter in the geometric optics limit. Rays were traced through the optics to many points in the focal plane and the size of the Lyot aperture stop reduced until every ray hit the primary mirror within 291 (projected) cm of its center. The illumination of the primary from any single field point does not quite fill 97% of the mirror diameter. This is because the Lyot stop is not a perfect image of the primary for all field angles; to make it so would degrade sky imaging performance, because the two imaging goals compete for control over the shape and position of the first lens.

The Lyot stops are 43, 64, and 91 wavelengths wide at 145, 215, and 280 GHz, respectively. This results in a significant amount of diffraction, so geometric analysis of the Lyot stop does not correctly predict the spillover. Radiation from point sources at the focal planes was traced backwards through the ACT optics using diffraction analysis to calculate the complex electric field at each surface. The intensity at each mirror surface but beyond the mirror's physical edge is considered spillover. A result for the primary and secondary mirrors from a typical field is shown in Figure 6. To redirect spillover onto the sky, each mirror is surrounded by a reflecting planar guard ring, oriented parallel to the plane of the mirror's edge.

The illumination patterns were used to calculate the percentage of power missing the

primary and secondary mirrors. For typical points in the 145 GHz field, 0.2% of power spills over at the primary and 0.6% at the secondary. The values are much smaller for the 215 and 280 GHz cameras. The spillover would be approximately twice as large without the guard ring. Decreasing the size of the Lyot stop to illuminate only 95%, 90% and 85% of the main mirror diameter would not significantly reduce spillover, because the main contribution is from faint diffraction into wide angles at the secondary mirror. Some diffraction from the edge of the Lyot stop misses the secondary mirror regardless of how much of the primary mirror is illuminated, barring unrealistically large guard rings on the secondary. There is therefore no great advantage in reducing the primary mirror illumination. We do not expect the calculated secondary spillover to be a problem, because the majority of it is reflected directly toward the sky.

5.C. *Tolerance analysis*

Calculations were undertaken to find out how accurately optical elements need to be placed. Position and angular displacements were varied for all optical elements. Other parameters varied were the refractive indices of lenses, the shapes of surfaces, and the temperature of the telescope. The size of the perturbations was increased until the rms wavefront error of a test pixel increased by 0.016λ (a reduction in the Strehl ratio of approximately 0.01). The results of these tests were compared to the results of dynamic finite element analysis (FEA) of the telescope structure produced by AMEC. In the following, note that a change in Strehl produces a proportionate change in the instrument’s forward gain.

The tolerancing tests were performed both with and without allowing refocusing of the telescope using the secondary mirror (see Section 3). All static misalignments predicted by FEA were easily corrected for by refocusing. We anticipate having to refocus with each change in elevation, according to a table to be built from beam maps made on bright, unresolved sources. Uniform temperature changes between -20°C and 20°C do not degrade optical performance. Temperature gradients cause changes in the Strehl ratio well below the expected level of variations in atmospheric transmission (and at slower timescales), with the possible exception of direct insolation on the panels in mid-day. More serious are the 1% Strehl changes expected when the telescope is accelerated at either end of each scan. These changes will be scan-synchronous and might require cutting some small fraction of the data.

Refocusing the secondary could correct for uncorrelated random positioning errors of every optical element in a single camera if the misalignments do not exceed 2 mm rms in displacement or 5° rms tilts. Unfortunately, though, one compromise correction must be made for all three cameras. Given this constraint, we find that MBAC’s optical elements need to be placed to within 1.5 mm and 2° of their nominal positions and orientations. Careful mechanical design will achieve these values. The one dimension of substantially tighter tolerance

is the spacing between the arrays and the coldest lenses (Lens 3). This distance must be accurate to 0.5 mm owing to the fast focus onto the detectors. Mounting the detectors and Lens 3 to a single metal structure will allow us to reach the required accuracy.

5.D. *Ghost images*

Light undergoing an even number of reflections from the nominally transparent lens and filter surfaces in MBAC can produce secondary (“ghost”) images. Provided that the intensity of such images is well below that of the diffraction-limited point spread function (PSF), their effect can be ignored. Where this is not the case, ghost images will act as extra sidelobes to the main beam. We have estimated ghosting effects using ray-tracing. For each pair of cold surfaces, 10,000 rays were traced through the system to the detector focal plane, and an image was built up by adding the ray intensities incoherently. Each ray was weighted by the reflectivity of the two surfaces from which it reflected. For simplicity, reflectivity was assumed to be independent of incident angle. Conservative (i.e. large) estimates were used: 3% reflection for the window, 4% for each lowpass filter, 2% for the bandpass filter, 10% for the array, and 1% per surface for the antireflection-coated lenses. To account for diffraction, the resulting ghost images were smoothed with the PSF of the main image.

Calculations for all fields in all three cameras gave results qualitatively similar to those shown in Figure 7. Reflections between closely spaced planar elements (such as the first three lowpass filters or the bandpass filter and the last lens) create a ghost coincident with the main image, resulting in a peak at approximately -28 dB, centered on the main PSF. This ghost is much less intense than the diffraction-limited main image and is of little consequence. Light reflected from the bandpass filter and any of several other lens or filter surfaces creates a much broader ghost image on the opposite side of the array from the main image, with amplitudes as high as -41 dB. Although this is brighter than the diffraction sidelobes of the main PSF at that distance, the diffuse ghost image will be below the noise of any anticipated integration except around the brightest point sources. With the conservative reflectivity estimates used in the present analysis, the ghost image’s integrated intensity is approximately 2% that of the main PSF. We expect a ghost image of this magnitude to be detectable during beam-mapping studies of bright, unresolved sources (e.g. planets), but ghosting will not be a problem for our planned CMB observations.

6. Conclusions

We have developed a diffraction-limited optical design that can be used to illuminate large arrays of millimeter-wave detectors. The design meets the requirements described in Table 1, and we have studied the system properties using geometric and diffraction analysis techniques. The Gregorian system described in this paper has been built in British Columbia

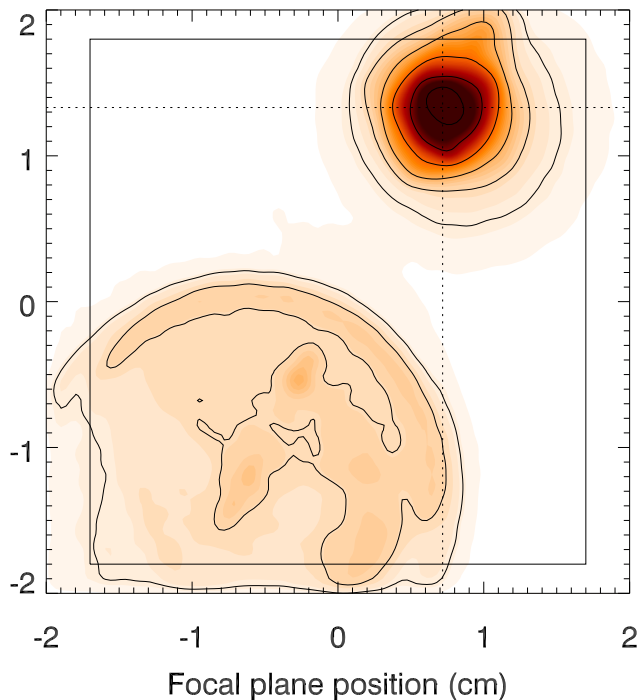


Fig. 7. (Color online) The secondary (ghost) images formed by stray light reflected twice from lens, filter, window, and array surfaces for a source imaged near the top of the 215 GHz detector array. The amplitude and shape of the ghost images shown here are typical of all fields, assuming conservative values for surface reflectivities. The dotted lines cross at the center of the main image (not shown). The dashed rectangle shows the extent of the focal plane array. The shading indicates the ghost image intensity on a linear scale relative to the peak of the main PSF, saturating at 5×10^{-4} ; the contours show intensities of -47 , -44 , -41 , -38 , -35 , and -32 dB relative to the main PSF. The ghost intensity peaks very near the main PSF at approximately -28 dB, where it is negligible. The diffuse ghost on the opposite side of the array reaches only -41 dB and is unlikely to affect CMB observations.



Fig. 8. The ACT telescope mostly assembled at AMEC in June 2006. The inner ground screen is not completed in this photograph.

(Figure 8). The 6-meter telescope is scheduled to be installed in Chile in early 2007. The cold optics are being built separately and will be installed on the telescope subsequently. A prototype camera with a cold optics design based on silicon lenses has been built and has observed astronomical sources using a Gregorian reflector much smaller than ACT.

ACT is a dynamic collaboration, and we thank all its members for many conversations and friendly debates. We especially thank Bob Margolis for his years as ACT project manager. We wish to thank employees of AMEC Dynamic Systems, KUKA Robotics, and Forcier Machine Design for their countless contributions to this project. We thank the Princeton Physics Machine Shop for their work on the design and construction of CCam. We gratefully acknowledge Mandana Amiri, Bryce Burger, Rolando Dunner, Norm Jarosik, Barth Netterfield, and Yue Zhao for thoughtful conversations about optics, telescope operation, and related detector matters, as well as for their collaboration in the lab and on-site at AMEC.

This work was supported by the U.S. National Science Foundation through awards AST-0408698 for the ACT project and PHY-0355328. Princeton University and the University of Pennsylvania also provided financial support. Some authors received additional support from 2004-2006 SPIE Educational Scholarships in Optical Science and Engineering (MN); an NSERC PGS-D scholarship (AH); Princeton University Centennial and Harold Dodds Fellowships (MN and TM); and an NSF Graduate Fellowship (TM).

References

1. J. W. Fowler, “The Atacama Cosmology Telescope project,” in *Millimeter and Submillimeter Detectors for Astronomy II*, J. Zmuidzinas, W. S. Holland, and S. Withington, eds., vol. 5498 of *Proc. SPIE*, pp. 1–10 (2004).
2. C. L. Bennett, M. Halpern, G. Hinshaw, N. Jarosik, A. Kogut, M. Limon, S. S. Meyer, L. Page, D. N. Spergel, G. S. Tucker, E. Wollack, E. L. Wright, C. Barnes, M. R. Greason, R. S. Hill, E. Komatsu, M. R. Nolta, N. Odegard, H. V. Peiris, L. Verde, and J. L. Weiland, “First-year Wilkinson Microwave Anisotropy Probe (WMAP) observations: preliminary maps and basic results,” *Astrophys. J. Suppl. Ser.* **148**, 1–27 (2003). [astro-ph/0302207](#).
3. C. L. Kuo, P. A. R. Ade, J. J. Bock, C. Cantalupo, M. D. Daub, J. Goldstein, W. L. Holzapfel, A. E. Lange, M. Lueker, M. Newcomb, J. B. Peterson, J. Ruhl, M. C. Runyan, and E. Torbet, “High-resolution observations of the cosmic microwave background power spectrum with ACBAR,” *Astrophys. J.* **600**, 32–51 (2004). [astro-ph/0212289](#).
4. E. M. Leitch, J. M. Kovac, N. W. Halverson, J. E. Carlstrom, C. Pryke, and M. W. E. Smith, “Degree Angular Scale Interferometer 3 year cosmic microwave background polarization results,” *Astrophys. J.* **624**, 10–20 (2005). [astro-ph/0409357](#).
5. W. C. Jones, P. A. R. Ade, J. J. Bock, J. R. Bond, J. Borrill, A. Boscaleri, P. Cabella, C. R. Contaldi, B. P. Crill, P. de Bernardis, G. De Gasperis, A. de Oliveira-Costa, G. De Troia, G. di Stefano, E. Hivon, A. H. Jaffe, T. S. Kisner, A. E. Lange, C. J. MacTavish, S. Masi, P. D. Mauskopf, A. Melchiorri, T. E. Montroy, P. Natoli, C. B. Netterfield, E. Pascale, F. Piacentini, D. Pogosyan, G. Polenta, S. Prunet, S. Ricciardi, G. Romeo, J. E. Ruhl, P. Santini, M. Tegmark, M. Veneziani, and N. Vittorio, “A Measurement of the angular power spectrum of the CMB temperature anisotropy from the 2003 flight of BOOMERANG,” *Astrophys. J.* **647**, 823–832 (2006). [astro-ph/0507494](#).
6. I. J. O’Dwyer, M. Bersanelli, J. Childers, N. Figueiredo, D. Halevi, G. Huey, P. M. Lubin, D. Maino, N. Mandolesi, J. Marvil, P. R. Meinhold, J. Mejía, P. Natoli, H. O’Neill, A. Pina, M. D. Seiffert, N. C. Stebor, C. Tello, T. Villela, B. D. Wandelt, B. Williams, and C. A. Wuensche, “The cosmic microwave background anisotropy power spectrum from the BEAST experiment,” *Astrophys. J. Suppl. Ser.* **158**, 93–100 (2005).
7. A. C. S. Readhead, B. S. Mason, C. R. Contaldi, T. J. Pearson, J. R. Bond, S. T. Myers, S. Padin, J. L. Sievers, J. K. Cartwright, M. C. Shepherd, D. Pogosyan, S. Prunet, P. Altamirano, R. Bustos, L. Bronfman, S. Casassus, W. L. Holzapfel, J. May, U.-L. Pen, S. Torres, and P. S. Udomprasert, “Extended mosaic observations with the Cosmic Background Imager,” *Astrophys. J.* **609**, 498–512 (2004). [astro-ph/0402359](#).
8. D. N. Spergel, L. Verde, H. V. Peiris, E. Komatsu, M. R. Nolta, C. L. Bennett, M. Halpern, G. Hinshaw, N. Jarosik, A. Kogut, M. Limon, S. S. Meyer, L. Page, G. S.

- Tucker, J. L. Weiland, E. Wollack, and E. L. Wright, “First-Year Wilkinson Microwave Anisotropy Probe (WMAP) observations: determination of cosmological parameters,” *Astrophys. J. Suppl. Ser.* **148**, 175–194 (2003). [astro-ph/0302209](#).
9. A. Kosowsky, “The future of microwave background physics,” in *AIP Conf. Proc. 666: The Emergence of Cosmic Structure*, S. H. Holt and C. S. Reynolds, eds., pp. 325–335 (2003).
 10. L. Verde and D. N. Spergel, “Dark energy and cosmic microwave background bispectrum,” *Phys. Rev. D* **65**(4), 043,007–+ (2002). [astro-ph/0108179](#).
 11. C. Hernández-Monteagudo, L. Verde, R. Jimenez, and D. N. Spergel, “Correlation properties of the kinematic Sunyaev-Zel’dovich Effect and implications for dark energy,” *Astrophys. J.* **643**, 598–615 (2006). [astro-ph/0511061](#).
 12. J. E. Carlstrom, G. P. Holder, and E. D. Reese, “Cosmology with the Sunyaev-Zel’dovich effect,” *Annu. Rev. Astron. & Astrophys.* **40**, 643–680 (2002). [astro-ph/0208192](#).
 13. K. M. Huffenberger and U. Seljak, “Prospects for ACT: simulations, power spectrum, and non-Gaussian analysis,” *New Astronomy* **10**, 491–515 (2005). [astro-ph/0408066](#).
 14. D. J. Benford, J. A. Chervenak, K. D. Irwin, and H. S. Moseley, “Ultralow-background large-format bolometer arrays,” in *IR Space Telescopes and Instruments*, J. C. Mather, ed., Proc. SPIE, pp. 944–953 (2003).
 15. T. A. Marriage, J. A. Chervenak, and W. B. Doriese, “Testing and assembly of the detectors for the Millimeter Bolometer Array Camera on ACT,” *Nucl. Instrum. Methods A* **559**, 551–553 (2006).
 16. M. J. Devlin, S. R. Dicker, J. Klein, and M. P. Supanich, “A high capacity completely closed-cycle 250 mK ^3He refrigeration system based on a pulse tube cooler,” *Cryogenics* **44**, 611–616 (2004).
 17. J. Lau, M. Benna, M. Devlin, S. Dicker, and L. Page, “Experimental tests and modeling of the optimal orifice size for a closed cycle He sorption refrigerator,” *Cryogenics* **46**, 809–814 (2006).
 18. M. J. Griffin, J. J. Bock, and W. K. Gear, “Relative performance of filled and feedhorn-coupled focal-plane architectures,” *Appl. Opt.* **41**, 6543–6554 (2002). [astro-ph/0205264](#).
 19. Optical Research Associates, 3280 East Foothill Blvd., Pasadena, California, 91107.
 20. C. Dragone, “A first-order treatment of aberrations in Cassegrainian and Gregorian antennas,” *IEEE Trans. Antennas Propag.* **30**, 331–339 (1982).
 21. C. Dragone, “First-order correction of aberrations in Cassegrainian and Gregorian antennas,” *IEEE Trans. Antennas Propag.* **31**, 764–775 (1983).
 22. K. Brown and A. Prata, “A design procedure for classical offset dual reflector antennas with circular apertures,” *IEEE Trans. Antennas Propag.* **42**(8), 1145–53 (1994).

23. H. Tanaka and M. Mizusawa, "Elimination of cross polarization in offset dual-reflector antennas," *Electronics Communications of Japan* **58**, 71–78 (1975).
24. D. Schroeder, *Astronomical Optics*, 2nd ed. (Academic Press, 2000).
25. M. Born and E. Wolf, *Principles of Optics*, 7th ed. (Cambridge, 1999).
26. AMEC Dynamic Structures, 1515 Kingsway Ave., Port Coquitlam, BC V3C 1S2, Canada.
27. KUKA Robotics Corporation, 2250 Key Drive, Clinton Township, Michigan, 48036.
28. Forcier Machine Design, 123 Marshall Ave., Petaluma, California 94952.
29. Faro Technologies Inc., 125 Technology Park, Lake Mary, Florida 32746.
30. W. V. T. Rusch, A. J. Prata, Y. Rahmat-Samii, and R. A. Shore, "Derivation and application of the equivalent paraboloid for classical offset Cassegrain and Gregorian antennas," *IEEE Trans. Antennas Propag.* **38**, 1141–1149 (1990).
31. P. A. R. Ade, G. Pisano, C. Tucker, and S. Weaver, "A review of metal mesh filters," in *Millimeter and Submillimeter Detectors and Instrumentation for Astronomy III*, J. Zmuidzinas, W. S. Holland, S. Withington, and W. D. Duncan, eds., vol. 6275 of *Proc. SPIE*, p. 62750U (2006).
32. C. E. Tucker and P. A. R. Ade, "Thermal filtering for large aperture cryogenic detector arrays," in *Millimeter and Submillimeter Detectors and Instrumentation for Astronomy III*, J. Zmuidzinas, W. S. Holland, S. Withington, and W. D. Duncan, eds., vol. 6275 of *Proc. SPIE*, p. 62750T (2006).
33. Emerson and Cuming, Billerica, Massachusetts, 01821.
34. V. V. Parshin, R. Heidinger, B. A. Andreev, A. V. Gusev, and V. B. Shmagin, "Silicon as an advanced window material for high power gyrotrons," *Int. J. Infrared Millimeter Waves* **16**(5), 863–877 (1995).
35. J. W. Lamb, "Miscellaneous data on materials for millimetre and submillimetre optics," *Int. J. Infrared Millimeter Waves* **17**(12), 1997–2232 (1996).
36. Siltronic AG, 81737 München, Germany.
37. J. Lau, J. Fowler, T. Marriage, L. Page, J. Leong, E. Wishnow, R. Henry, E. Wollack, M. Halpern, D. Marsden, and G. Marsden, "Millimeter-wave antireflection coating for cryogenic silicon lenses," *Appl. Opt.* **45**, 3746–3751 (2006).
38. M. D. Niemack, "Measuring two-millimeter radiation with a prototype multiplexed TES receiver for ACT," in *Millimeter and Submillimeter Detectors and Instrumentation for Astronomy III*, J. Zmuidzinas, W. S. Holland, S. Withington, and W. D. Duncan, eds., vol. 6275 of *Proc. SPIE*, p. 62750B (2006).
39. S. Dicker and M. Devlin, "Millimeter wave reimaging optics for the 100 m Green Bank Telescope," *Appl. Opt.* **44**, 5855–5858 (2005).